aerospace

MDPI

Article

Preliminary Analysis of the Performance of an Electric Supersonic Propeller

Jens Kunze *,† **and Allan Paull** †

Centre for Hypersonics, The University of Queensland, Brisbane, QLD 4072, Australia; allan.paull@uq.edu.au
* Correspondence: j.kunze@uq.edu.au
† These authors contributed equally to this work.

Abstract: A preliminary aerodynamic and thermodynamic analysis of a supersonic propeller driven by an electric motor is performed. The analysis is aimed at determining whether such a system is feasible and further and more detailed investigation is warranted. Recent progress in electric energy storage and motors, as well as high temperature and lightweight materials, has opened up the design space for a large number of applications. Electrically powered flight and propellers are among these applications. This study shows that very good aerodynamic and propulsive efficiencies can be achieved with this combination. In this paper, the design space of supersonic propeller blades is explored and the effect of a number of design parameters on the blade efficiency is shown. Further analysis is performed to demonstrate that reasonable efficiency can be achieved at flight Mach numbers from two to six between 15 and 35 km altitude. Finally, a mission-based propeller design study is performed to demonstrate practical system performance and show trade-offs between different parameters.

Keywords: supersonic propeller; supersonic electric propulsion

Citation: Kunze, J.; Paull, A. Preliminary Analysis of the Performance of an Electric Supersonic Propeller. *Aerospace* **2023**, *10*, 803. https://doi.org/10.3390/aerospace10090803

Academic Editor: Jae Hyun Park

Received: 22 August 2023
Revised: 6 September 2023
Accepted: 7 September 2023
Published: 14 September 2023

1. Introduction

Electric modes of transportation have become ubiquitous in today's modern societies. From small personal transport devices over electric cars to trains and even cargo ships, combustion-based systems are repeatedly being replaced by electric systems. In addition to that, completely new transportation devices have been made possible by attaching electric motors to bicycles, skateboards and virtually anything with wheels. Concurrently, battery technology has progressed to provide higher specific energy and higher specific power, i.e., energy and power per unit mass, and higher energy density and higher power density, i.e., energy and power per unit volume. This development is projected to continue for the foreseeable future.

As far as electric flight is concerned, drones and other remote controlled aircraft have surpassed the state of simply being used by hobbyists and have found numerous applications in a variety of industries. Indeed, even small low-speed short distance electric passenger aircraft are already a reality. However, electric high-speed and supersonic flight have not been achieved to date. The biggest hurdles are the aforementioned specific power and specific energy of electric energy storage systems (EESS). Figure 1 shows the typical specific power over the specific energy of different EESS.

The plot demonstrates the general characteristics for common EESS. There appears to exist a trade-off between specific energy and specific power, with Li-ion batteries and supercapacitors occupying the regions most relevant for flight. Typically, batteries have higher specific energy and supercapacitors higher specific power.

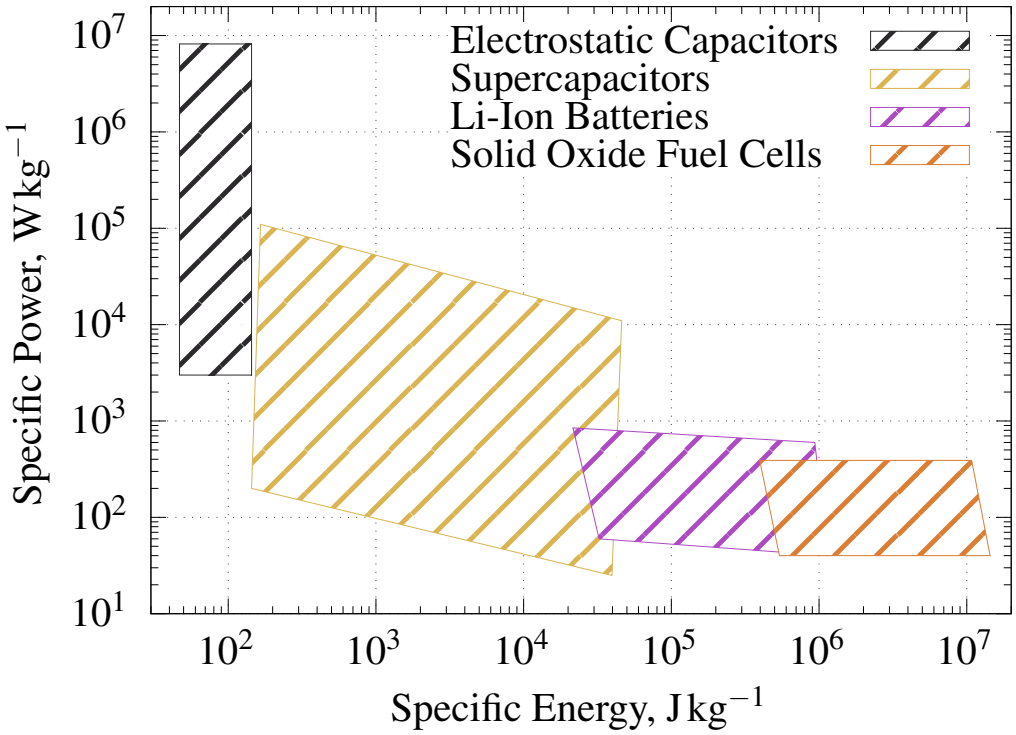

Figure 1. Typical specific power over specific energy for different electric energy storage systems, reproduced from [1].

Contemporary batteries are still too large and too heavy to compete with combustion based systems; state-of-the-art lithium-ion batteries have a specific energy of approximately 1 MJ/kg compared to 43 MJ/kg for common jet fuels. However, considering the current momentum of progress in battery technology, see for instance [2–5] or a recent press release from industry (https://news.samsung.com/global/samsung-presents-groundbreaking-all-solid-state-battery-technology-to-nature-energy (accessed on 11 September 2023)), this gap will likely be much smaller in the near future, in particular when the high efficiency of an electric system is accounted for.

As far as specific power goes, model aircraft and drone battery manufacturers already claim to be able to achieve discharge currents greater than 1000 A or 24 kW kg^{-1} (https://www.rccaraction.com/turnigy-alpha-140c-premium-hardcase-lipo-battery-packs/ (accessed on 11 September 2023)). A recent experimental analysis [6], however, demonstrates that approximately 300 A, or 7 kW kg^{-1}, for around 30 s are realistically achievable with these batteries. Supercapacitors have been shown to reach even higher values [1,7].

Given these developments, it becomes reasonable to investigate the performance of propulsion systems that use electric energy sources. The most straightforward approach to convert electric energy into aerodynamic thrust is a propeller. Figure 2 shows a sketch of a simple propeller-driven vehicle, consisting of a nose cone, the propeller and a boat tail.

The engine station numbering is chosen to be consistent with common jet engine notation, where station 0 indicates freestream quantities, station 1 is just upstream of the inlet, station 2 is just upstream of the compressor, station 5 is just behind the turbine and station 9 designates the flow conditions just downstream of the engine. In this study, the power efficiency, propeller blade temperature and mechanical loads of such a system are evaluated to determine its feasibility.

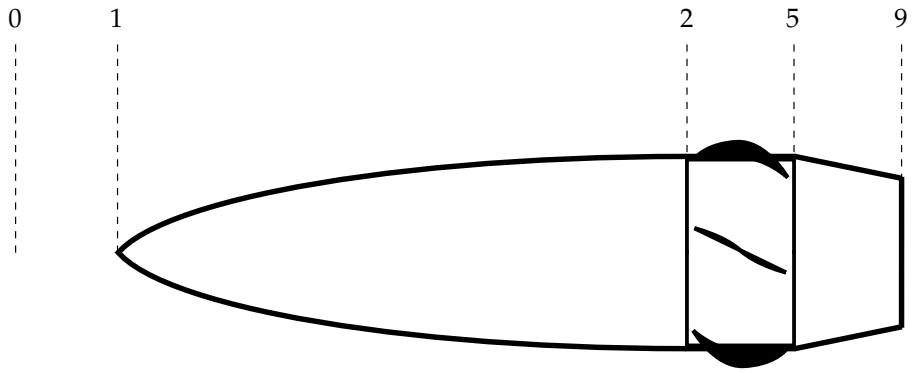

Figure 2. A sketch of a propeller behind a nose cone and with a boat tail. The numbers indicate reference stations.

2. Materials and Methods

In this analysis, the flow is assumed to be two-dimensional and the flow conditions on either side of a propeller blade are calculated with shock-expansion theory [8]. It is assumed that this provides sufficient detail and that the interactions between shocks and expansion waves, which would require a more sophisticated flow model, are either small enough to be ignored or do not affect the flow on the propeller blades. Skin friction, boundary layer thicknesses and blade temperatures are calculated using the reference temperature method [9] combined with semi-empirical relations for the boundary layer thicknesses ([10], Appendix B, pp. 337–350).

For the majority of calculations, the gas is modelled as a perfect gas with $\gamma = 1.4$. However, for the calculation of the propeller blade wall temperature, the specific heats, thermal conductivity and viscosity are assumed to be temperature-dependant. The properties were calculated using the equations from McBride and Gordon ([11], pp. 19–21) for air with the following composition: 78.1 % N_2, 20.9 % O_2, 0.94 % Ar and 0.032 % CO_2 by volume. The material constants for the equations for the specific heats, thermal conductivity and viscosity can be found in McBride and Gordon [12].

Figure 3 shows a sketch of a 2D flat plate propeller blade with velocity triangles upstream and downstream of the blade.

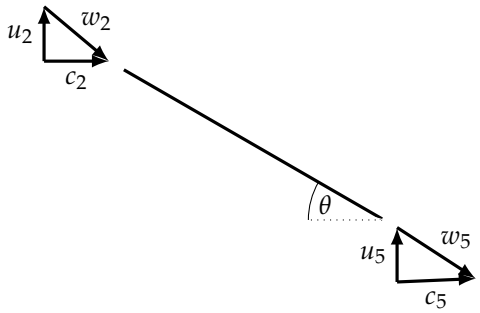

Figure 3. A sketch of a 2D propeller blade with velocity triangles.

The nomenclature is based on one commonly used in turbomachinery, where c indicates absolute velocities, u the rotational velocity and w relative velocities. Note that only w is in a blade relative coordinate frame and both c and u are in a vehicle fixed frame. The angle θ is the cord angle of the blade, which is measured relative to the freestream. The number of blades on a propeller is denoted by n_b. A useful quantity is the velocity ratio, which is defined as

$$v_r = \frac{u_2}{c_0} \,. \tag{1}$$

It can be used to compare the performance of propeller blades across propeller hub radii, rotational speeds and blade angles.

In Figure 3, a shock will form on the top (windward) side of the blade and an expansion forms on the bottom (leeward) side. The resulting pressure difference causes a force across the blade, which accelerates the vehicle. The propeller cannot produce any thrust if $v_r < \tan(\theta)$ because the shock will form on the opposite side and the resulting pressure difference across the blade will decelerate the vehicle. Note that this effect can potentially be used to enhance the manoeuvrability of the vehicle by using the propeller as a break. With the electric motor acting as a generator the EESS can be recharged too. At $v_r = \tan(\theta)$ the pressure on either side of the blade is the same.

2.1. System Efficiency

The power efficiency is defined as the ratio of thrust power to the power delivered by the propeller, i.e.,

$$\frac{P_T}{P_M} = \frac{c_0 F_z}{\omega M_T}\,, \tag{2}$$

where F_z designates the component of the force parallel to the axis of symmetry of the vehicle in Figure 2, ω indicates the angular velocity of the propeller and M_T designates the torque of the electric motor. The thrust power is indicated by P_T and the mechanical power of the motor by P_M. Using the efficiency of the electric motor and accounting for losses between the motor and the EESS, the required power output of the EESS can be calculated:

$$P_E = \zeta P_M\,, \tag{3}$$

where ζ designates the combined efficiency of the electric system.

2.2. Blade Models

Three types of blades are being investigated in this study. As the flow is assumed to be 2D, the blades are specified by defining a blade cross-section and a blade height. In Figure 4 the blade types are shown.

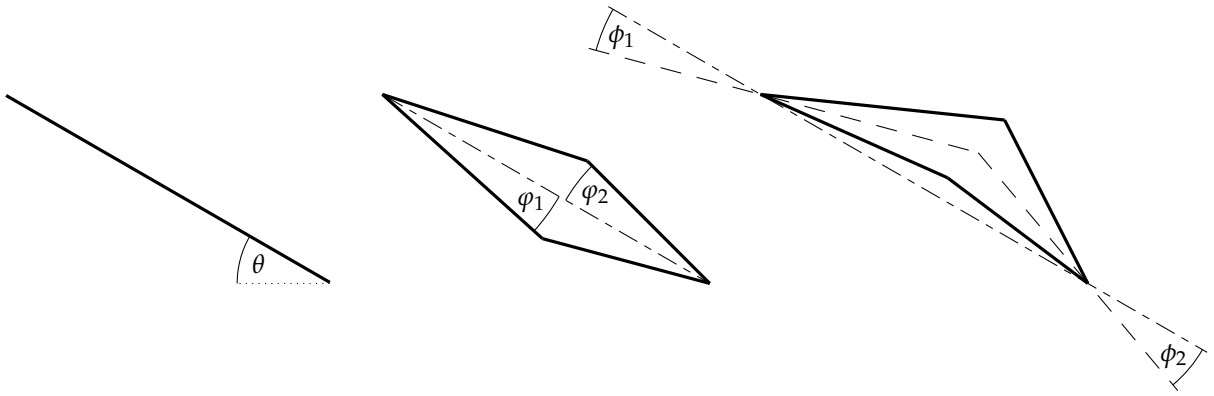

Figure 4. A sketch of an example of each of the three blade types used in this analysis.

Namely, a flat plate blade, a diamond-shaped blade and a generic four-sided blade. These shapes are chosen because a flat plate is the optimal shape for a lifting body in supersonic flow, a diamond cross-section approaches the efficiency of a flat plate but can be made structurally stronger and is, therefore, used for wings of supersonic aircraft. The generic four-sided blade is used to determine whether the efficiency of a flat plate can be exceeded with a more complex geometry.

For each blade, the cord is defined as the straight line connecting the leading edge to the trailing edge. Its inclination to the freestream direction is given by the cord angle θ and its length is the cord length l_c. Together with the blade height h_b, these parameters are sufficient to define a flat plate blade. The diamond and generic blades consist of two intersecting wedges, which are anchored at the edges. Their shape is defined by the wedge half angles φ_1 and φ_2. For the generic blade, the wedge axis angles ϕ_1 and ϕ_2 give the

inclination of each wedge with respect to the cord. The generic blade allows for a large variety of blade cross-sections to be created. In the following, to be able to distinguish between different blades, a diamond-shaped blade with $\varphi_1 = 2°$ and $\varphi_2 = 5°$ will be referred to as a 2-5 diamond. A generic blade with $\phi_1 = 3°$, $\phi_2 = 6°$, $\varphi_1 = 2°$ and $\varphi_2 = 5°$ will be referred to as a 3-6-2-5 generic blade. Note there are two constraints to ensure that a generic blade is physically possible, i.e.,

$$(\phi_1 + \varphi_1) \cdot (\phi_2 + \varphi_2) \geq 0 \qquad \text{and} \tag{4}$$

$$(\phi_1 - \varphi_1) \cdot (\phi_2 - \varphi_2) \geq 0, \tag{5}$$

where $\varphi_1 \geq 0$, $\varphi_2 \geq 0$ and ϕ_1 and ϕ_2, respectively, are positive when the respective wedge axis is tilted towards the windward side of the blade and negative when the respective wedge axis is tilted towards the leeward side, i.e., in Figure 4 both ϕ_1 and ϕ_2 are positive. If either (4) or (5) are equal to zero, two sides of the four-sided blade coincide with the cord and it becomes effectively three-sided.

2.3. Wall Temperature Calculation

To calculate the blade temperature, it is assumed that the propeller blades are in radiation equilibrium, i.e.,

$$\epsilon\sigma T_w^4 - k \left.\frac{\partial T}{\partial y}\right|_w = 0\,, \tag{6}$$

where the temperature gradient in the boundary layer near the wall is replaced by a finite difference:

$$-k \left.\frac{\partial T}{\partial y}\right|_w = -k \frac{T_{aw} - T_w}{\delta_c}\,. \tag{7}$$

Here, T_w designates the wall temperature, T_{aw} indicates the adiabatic wall temperature, k designates the thermal conductivity of the air near the blade surface, ϵ designates the emissivity of the blades and σ indicates the Stefan–Boltzmann constant. A conservative estimate of $\epsilon = 0.5$ is used in this study. The characteristic boundary layer thickness δ_c is used as the length scale for the finite difference. This entire system of equations has to be solved iteratively. An implementation of the Newton method [13] is used here.

2.4. Validation

In order to validate the models described in this section, some flat plate calculations are compared to the experimental results. Figure 5 shows the calculated skin friction coefficient compared to measurements made by Cole [14] and the calculated Stanton number compared to measurements made by Chang ([15], pp. 65–66). The denominations M7B and M7.7B in Figure 5b refer to specific experiments performed by Chang.

The Stanton number is calculated using

$$St = \frac{q_w}{\rho_e u_e c_{p,e} (T_{aw} - T_w)}\,, \tag{8}$$

where q_w is the heat flux at the wall and ρ_e, u_e and $c_{p,e}$ are the density, velocity and specific heat at constant pressure at the edge of the boundary layer. The laminar skin friction coefficient and Stanton number compare well to the experimental data. As far as the turbulent calculations are concerned, there is a noticeable difference to the experimental data; however, the calculations provide a reasonable approximation. The effects of boundary layer transition on both the skin friction coefficient and the Stanton number cannot be reproduced since transition is modeled to be instantaneous.

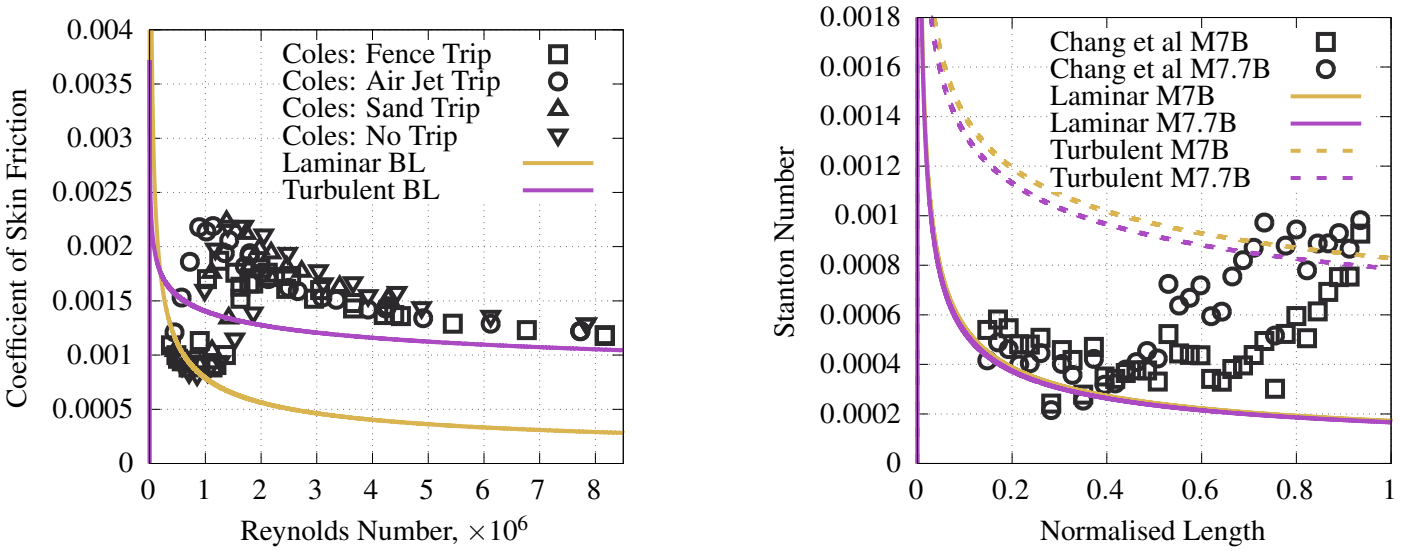

(**a**) (**b**)

Figure 5. Validation of the viscous calculations by comparison with experimental data. (**a**) shows the validation of the coefficient of skin friction and (**b**) shows the validation of the heat transfer model.

3. Results

In the first part of this section, a variety of blades are evaluated to determine the influence of a number of parameters on the power efficiency. It serves to establish an approximate performance maximum, a rough design guideline and the operational envelope of flight conditions. In the second part, a propeller is designed for a specific set of constraints of a mission. To find the optimal blade, a vehicle-level analysis has to be performed to balance all the relevant parameters with the mission requirements.

3.1. Propeller Blade Performance

The parameters of the standard configuration, blade and propeller hub dimensions and flight conditions, used in the following are shown in Table 1.

Table 1. The standard blade and flight conditions.

Type	l_c, mm	h_b, mm	θ, °	r_h, mm	Altitude, km	Mach Number
Flat Plate	100	30	30	185	15	4

Unless otherwise indicated, the standard blade was used. In the analysis below, where the effect of individual parameters is investigated, only the parameter in question is changed and the others remain as for the standard blade.

Figure 6a shows a comparison of the inviscid power efficiency with the viscous power efficiency of the standard configuration. The thrust power of the viscous blade is also shown. As is evident, the inviscid power efficiency approaches 1 where $v_r = 0.577$. At this point, $\tan^{-1}(v_r) = \theta$, i.e., w_2 is parallel to the blade. Here, the blade cannot produce any thrust as there is no pressure difference across it; thus, the net force is zero. The viscous efficiency and thrust power at this point are actually negative because the viscous forces oppose the forward motion of the vehicle and the rotation of the propeller, i.e., the motor has to deliver power to maintain its speed, but the vehicle is accelerated backwards. Viscous effects become less significant at higher v_r because the magnitude of the inviscid forces increases relative to the magnitude of the viscous forces. From an operational point of view this has important implications since a small change in conditions can result in a very large difference in power efficiency, and, in fact, a complete loss of thrust, at lower v_r. The same change in conditions at higher v_r, however, is of little consequence. However,

operational safety has to be balanced with efficiency and, as Figure 6b shows, increasing blade temperatures.

Note that the range of $0.58 \leq v_r \leq 0.8$ is equivalent to 33 krpm to 45 krpm, i.e., quite a large operational range. At $v_r = 0.58$ there is no discernible difference in temperature between the windward (WS) and the leeward side (LS). Both the temperature difference between the two sides as well as the magnitude of the temperature on either side increase with v_r. The jump in temperature on the windward side at $v_r = 0.80$ is caused by boundary layer transition. As the transition region itself is not modelled, there is a sharp rise in temperature and the flow model assumes a fully turbulent boundary layer instantaneously. What transition means for the performance of the blade is unclear at this point and cannot be determined with this level of analysis.

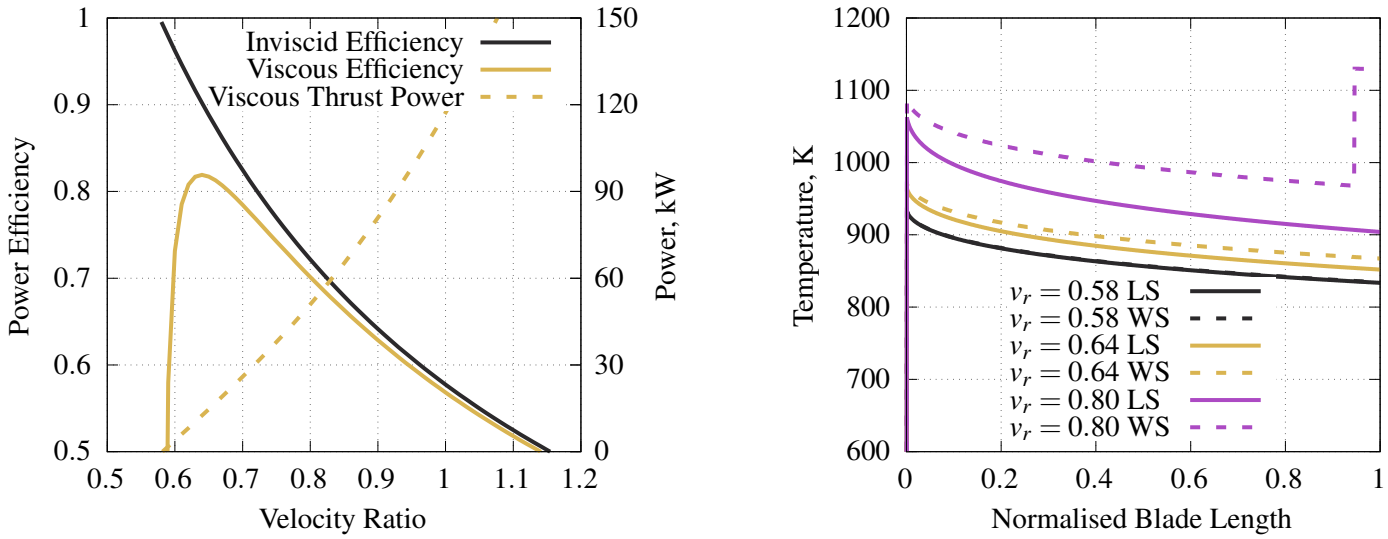

(**a**) (**b**)

Figure 6. (**a**) the viscous and inviscid power efficiency of the standard blade together with the thrust power of the viscous blade and (**b**) the blade temperature distribution at three different v_r.

3.1.1. Geometric Parameters

First, the blade type is investigated. In Figure 7, five examples of diamond-shaped blades are compared to a flat plate blade. The flat plate outperforms any of the diamond-shaped blades, as shown in Figure 7a. However, for very shallow half-wedge angles, the difference is quite small, i.e., the loss in efficiency is less than 10% up to a 3-3 diamond. It is interesting to note that both the 1-5 diamond and the 5-1 diamond are more efficient than the 3-3 diamond. This suggests that asymmetric diamonds, i.e., where $\varphi_1 \neq \varphi_2$, can have advantages over symmetric ones.

The peak temperature at the leading edge on the windward side of each blade is a function of shock strength. The shock strength depends on the velocity ratio and the half-wedge angle φ_1 at the leading edge. A larger φ_1, furthermore, contributes to a larger discrepancy between the blade temperature on the windward and the leeward side. Generally speaking, the wall temperature is higher the lower the power efficiency of a blade. Figure 7b demonstrates these effects by comparing the flat plate blade temperature to that of the 5-5 diamond. The location of the corners in the diamond profile can clearly be seen by the jump in wall temperature.

A shape optimisation using sequential least squares programming for non-linear constrained optimisation problems [16] was used to confirm the observations made with Figure 7, namely, that a flat plate of infinitesimal thickness performs better than a diamond-shaped blade regardless of φ_1 and φ_2. In fact, an optimisation of the generic four sided blade converged to a flat plate too. Thus, it can be concluded that, under the assumptions made in this analysis, a flat plate blade provides the highest efficiency of the types investigated.

Note that the generic blade type is quite variable and can assume a large number of different geometries. It is, thus, unlikely that even more complex blade shapes would perform better than a flat plate.

The second parameter under investigation is the cord length. Figure 8 shows the power efficiency and blade temperatures at maximum efficiency of five blades ranging from $l_c = 25\,\text{mm}$ to $l_c = 500\,\text{mm}$.

There is a clear increase in efficiency with increasing cord length, with the efficiency increase per unit length added decreasing with increasing cord length. The increase is owed to the fact that the inviscid forces increase linearly with cord length in the given analysis; however, the viscous forces do not. In fact, for very long blades, the skin friction coefficient reduces to the point that any further increase in length will result in a negligible viscous force increment. An infinitely long blade will, therefore, approach the efficiency of the inviscid blade shown in Figure 6a. Obviously, there is a practical limit to the cord length and the optimum will be affected by more than just the power efficiency. The temperature distributions in Figure 8b show, for instance, that transition already occurs on both sides of the blade for $l_c = 200\,\text{mm}$, as seen by the sharp increase in temperature.

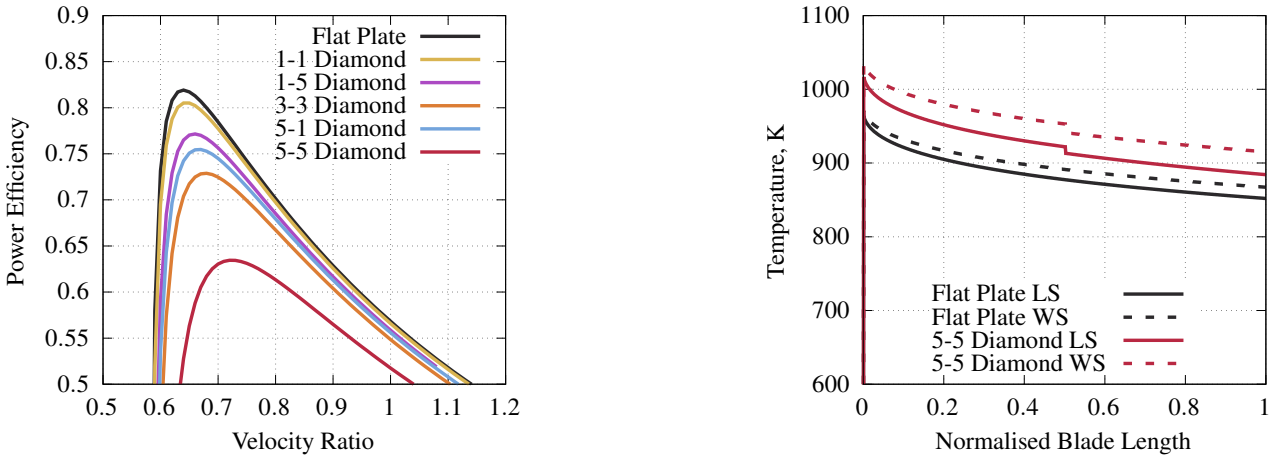

(**a**) (**b**)

Figure 7. A comparison of five diamond-shaped blades and a flat plate blade. (**a**) shows the power efficiency of each blade and (**b**) shows the wall temperature distribution of the flat plate blade and the 5-5 diamond blade.

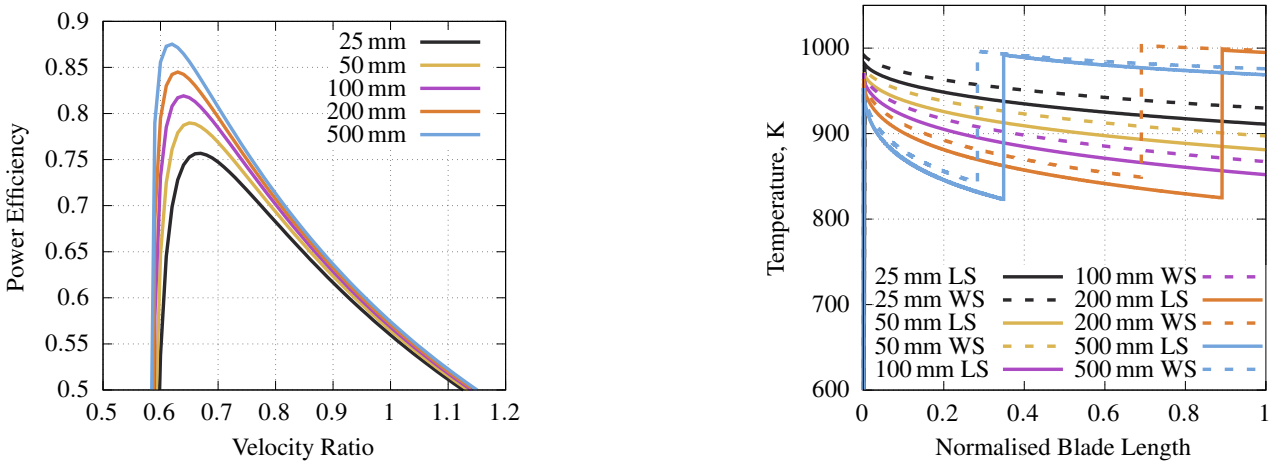

(**a**) (**b**)

Figure 8. The effect of varying l_c on the power efficiency and the temperature distribution at maximum efficiency. (**a**) shows the power efficiency of each blade and (**b**) shows the wall temperature distributions.

In Figure 9, the effects of varying the cord angle are shown.

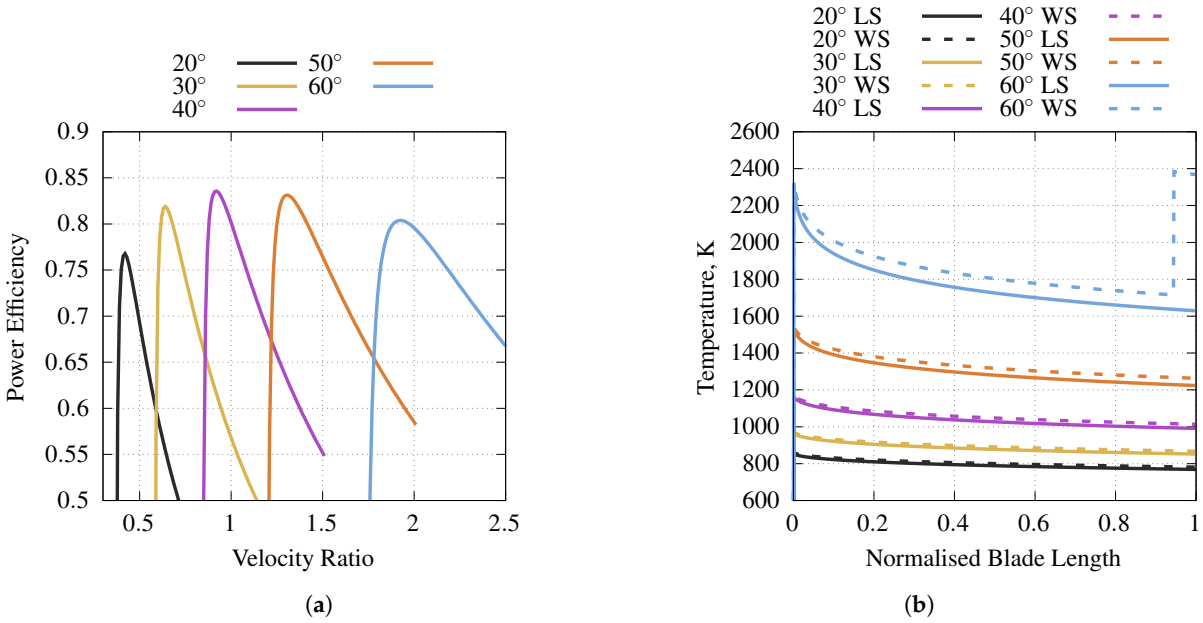

Figure 9. The effect of varying θ on (**a**) the power efficiency and (**b**) the temperature distribution at maximum efficiency.

Reducing the cord angle reduces the velocity ratio at which the propeller can produce thrust. The maximum power efficiency is achieved between 40° and 50°. Cord angles larger than 50° are not feasible because the wall temperature becomes too high, as Figure 9b shows; contemporary fibre reinforced ceramics can withstand temperatures of approximately 1500 K for extended periods of time.

Varying the hub radius has no effect on either the power efficiency with respect to the velocity ratio or the temperature distribution on the blade. However, it does affect the requirements for the electric motor. The power of the motor is the product of rotational speed and torque, i.e., the same amount of power can be delivered using high torque and low rotational speed or low torque and high rotational speed. The hub radius dictates which combination of the two is required to achieve a given velocity ratio and, therefore, desired efficiency. In Figure 10, the motor torque over rotational speed is shown for five different r_h.

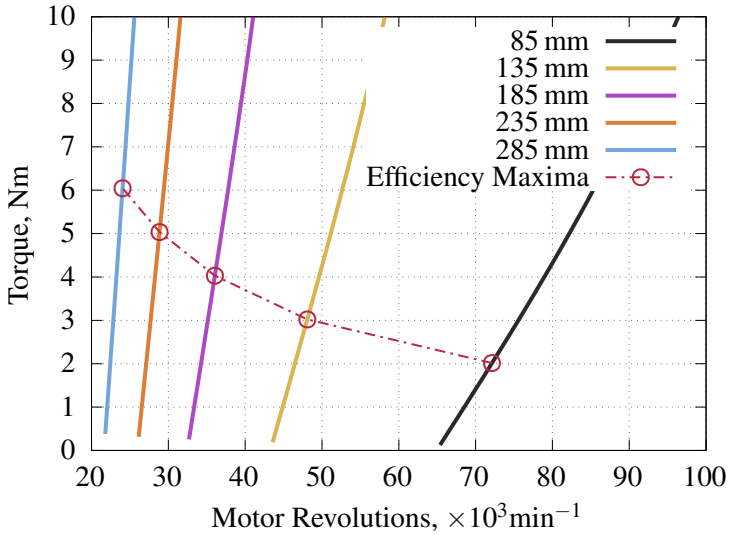

Figure 10. The effect of varying the hub radius on the requirements for the electric motor.

The location of the efficiency maxima is indicated to show how a linear change in hub radius affects the requirements for the motor. Note that the numbers shown are for a single propeller blade. For a real system the torque has to be multiplied by the number of blades while the rotational speed of the motor stays the same.

3.1.2. Flight Conditions

Figure 11 shows that, as far as power efficiency and blade temperature are concerned, the propeller is suited to flight at up to 35 km at Mach 4.

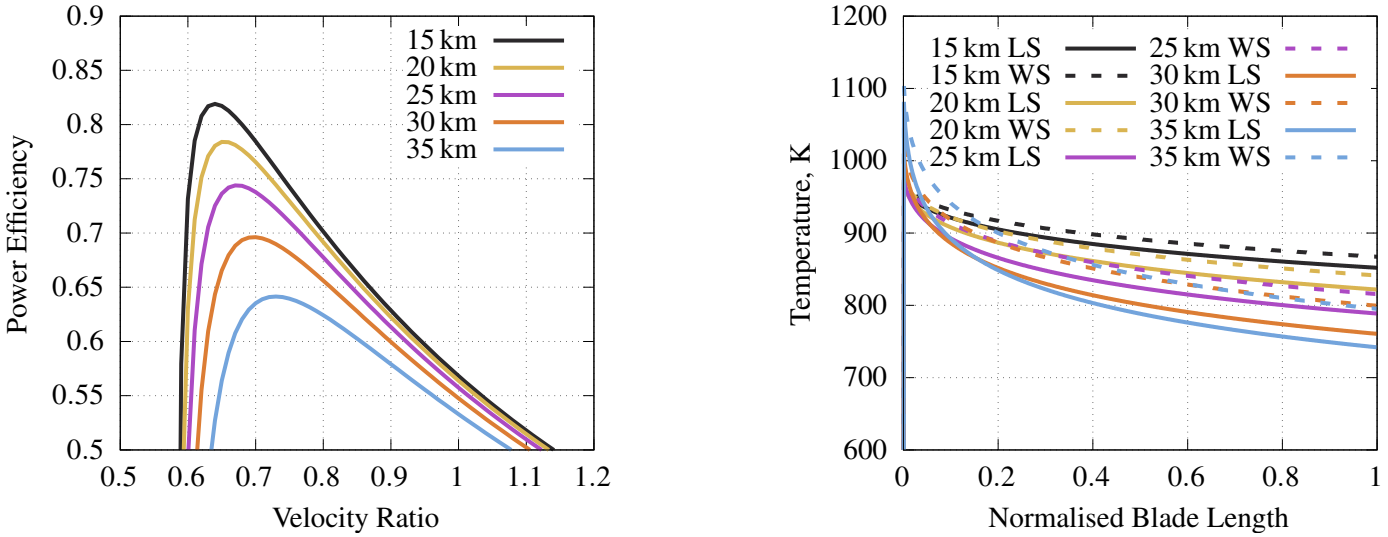

(**a**) (**b**)

Figure 11. The effect of flying at different altitudes on (**a**) the power efficiency and (**b**) the temperature distribution at maximum efficiency.

While there is a very significant drop in efficiency, the standard blade still achieves well over 60 % power efficiency. The temperature distributions in Figure 11b show the competing effects of a higher velocity ratio and a lower density. At the leading edge the boundary layer is equally small regardless of the flight altitude. The wall temperature is, thus, only a function of the flow temperature near the wall. Since the efficiency maximum at 35 km is at a higher velocity ratio than at the other altitudes, the shock at the leading edge is strongest and the wall temperature peak is the highest. Further along the blade, the high density at 15 km dominates the heat transfer to the blade; hence, the lowest altitude results in the highest temperature for most of the blade length. A higher freestream density results in a higher Reynolds number, which causes the boundary layer to be thinner and the heat transfer, thus, to be higher. However, none of the blade temperatures shown appear to be problematic.

As far as the flight Mach number is concerned, Figure 12 shows that it has a much smaller effect on the power efficiency than the flight altitude.

Very good power efficiencies can be achieved over the entire Mach number range shown in Figure 12. The blade temperature, however, limits the speed to approximately Mach 5.5 at 15 km.

An increase in altitude causes a drop in density and, thus, a thickening of the boundary layer. The thicker boundary layer causes higher viscous drag. This, in turn, significantly affects the power efficiency at lower velocity ratios where the total forces are lower. The efficiency maximum, thus, moves to a higher velocity ratio, where the angle of attack is higher and the leading edge shock is stronger. The combination of a higher angle of attack with higher viscous drag causes the total reduction in efficiency. An increase in Mach number, on the other hand, creates a stronger shock at the leading edge; however, it increases the Reynolds number at the same time, which reduces the boundary layer

thickness and, therefore, the viscous drag. Since the two effects are competing, the reduction in power efficiency is smaller than for the change in altitude.

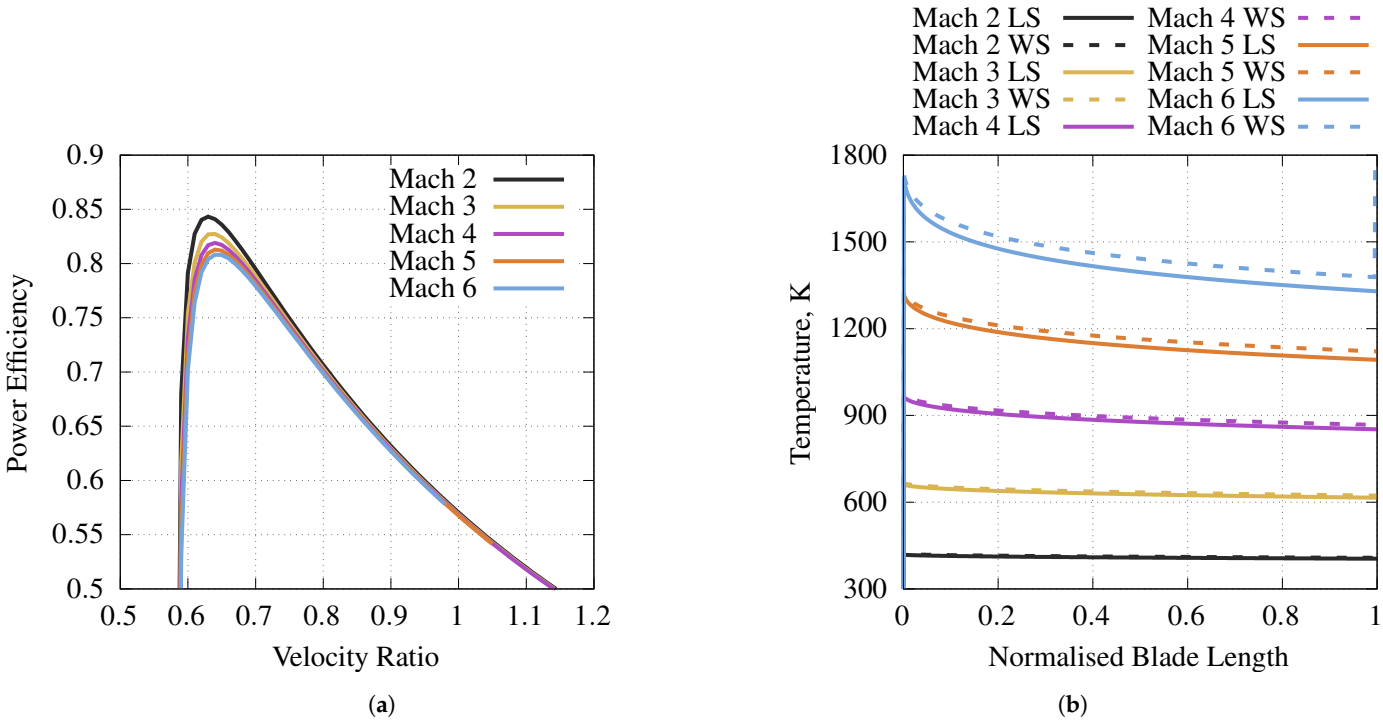

(**a**) (**b**)

Figure 12. The effect of the flight Mach number on (**a**) the power efficiency and (**b**) the temperature distribution at maximum efficiency.

Figure 13 shows the maximum power efficiency achievable with the standard blade with a variable cord angle for a variety of flight conditions. Each data point was calculated by optimising the cord angle at the given velocity ratio and flight condition. The plots serve to show at which conditions reasonable power efficiencies can be achieved.

The same curves can be obtained by connecting the peaks of the curves in Figure 9a. It is clear that, purely based on power efficiency, the standard blade allows for a very wide range of operation, assuming that a power efficiency of 0.6 is acceptable. Keep in mind that the temperature at Mach 6 is too high for the materials mentioned; although, this may change in the future. In fact, the reason that the curves on the Mach 5 and the Mach 6 plot are shorter than the other three is that the gas model is limited to 5000 K.

Note, that the blade angle of attack varies only slightly over a large range of velocity ratios; the largest increase at Mach 2 and 35 km is only 1.2° between velocity ratios of 0.1 and 2.5. For the design of a three-dimensional blade, this indicates that the blade should be twisted to keep the angle of attack constant for optimal performance since the velocity ratio of the standard blade varies by approximately 0.1 from the blade root to its tip. It can also be interpreted to mean that a blade without any twist will be close to optimum performance if h_b is sufficiently small. These assertions of course do not include any three-dimensional flow effects and they may well be outweighed by them.

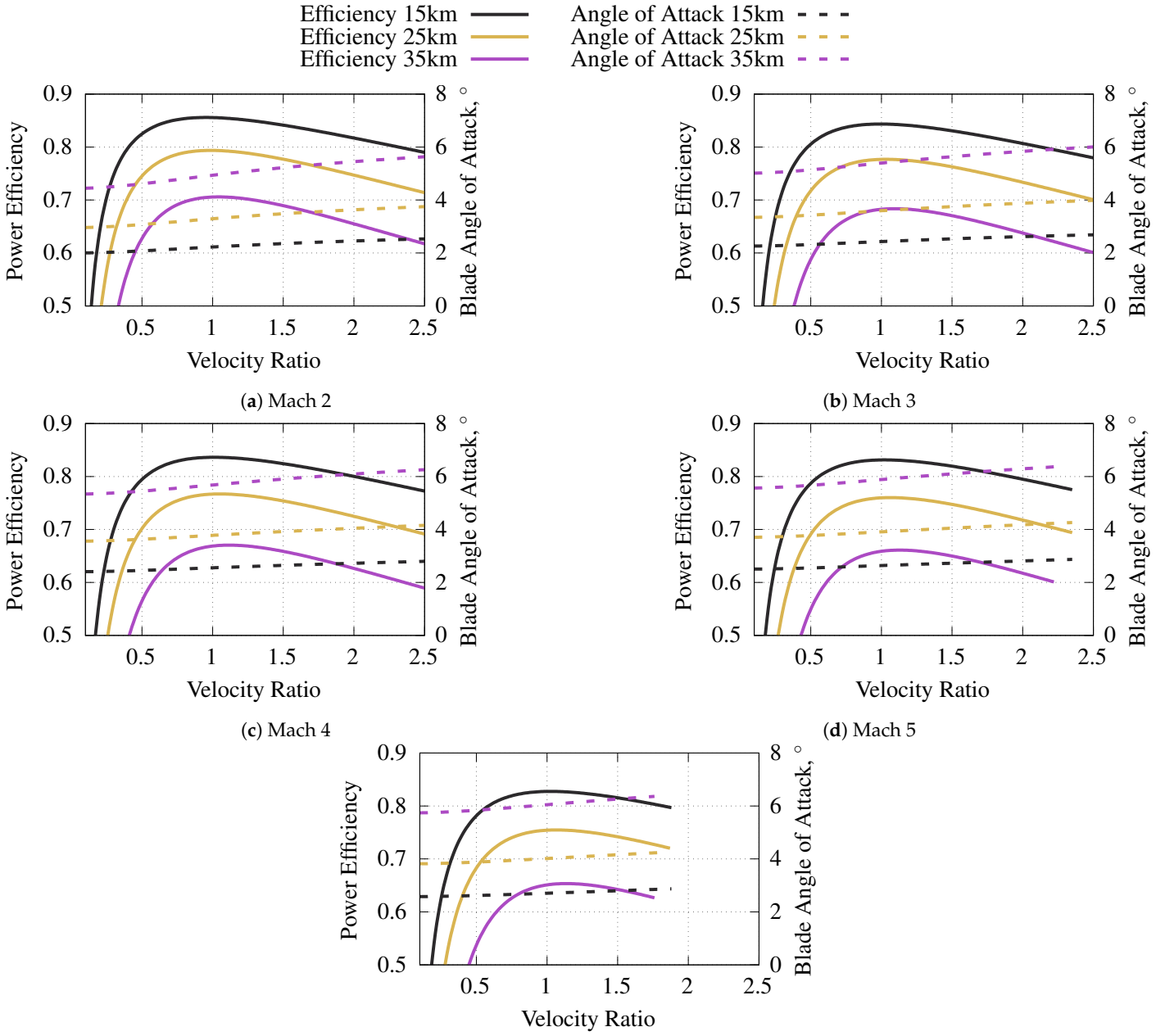

(**a**) Mach 2

(**b**) Mach 3

(**c**) Mach 4

(**d**) Mach 5

(**e**) Mach 6

Figure 13. Power efficiencies and the blade angle of attack at the optimal cord angle for a given velocity ratio at (**a**) Mach 2, (**b**) Mach 2, (**c**) Mach 2, (**d**) Mach 5 and (**e**) Mach 6 and 15 km and 35 km altitude.

3.2. Mission-Based Propeller Design

The previous section served to identify general performance trends related to a variety of design parameters. While these can provide useful insights, the comparison of a 500 mm-long blade to a 25 mm-long blade with all other parameters being equal is of little practical use. In order to assess the trade-offs between different parameters, a design target has to be specified and a number of propellers satisfying the target have to be designed. Thus, in this section a propeller is designed subject to a number of constraints, with the aim of achieving maximum efficiency, a maximum blade temperature of 1500 K and a purely laminar boundary layer on the propeller blades. Table 2 lists the complete set of design constraints. On this basis, the required thrust is calculated to which a propeller can be designed.

Table 2. The constraints for the propeller design.

Attribute	Value	Unit
Mission Type	Cruise	-
Vehicle Mass	65	kg
Mach Number	4	-
Altitude	15	km
Range	200	km
max. Motor Torque	35	Nm
max. RPM	50	$10^3\,\mathrm{min}^{-1}$

The maximum lift over drag a supersonic vehicle can achieve is commonly expressed using

$$\left.\frac{L}{D}\right|_{max} = \frac{4(M_0+3)}{M_0}\,. \tag{9}$$

Anderson et al. [17] have confirmed that Equation (9) provides a conservative estimate for lift over drag and can be exceeded by, for instance, wave riders. Equation (9) yields that, at Mach 4, $L/D = 7$ is achievable. To allow for some design flexibility, $L/D = 5$ is used here. The thrust required to achieve cruise at a constant altitude can, thus, be calculated:

$$T = \frac{m \cdot g}{L/D} = \frac{65\,\mathrm{kg} \cdot 9.81\,\mathrm{m/s^2}}{5} = 127.5\,\mathrm{N}\,. \tag{10}$$

At the given altitude and Mach number, 150 kW of thrust power are required for this mission.

In order to determine which combination of parameters satisfies and is best suited for the specified requirements, a parameter sweep was performed. Propellers with each possible combination of n_b and θ were designed, where $4 \leq n_b \leq 12$ and n_b is even and $20° \leq \theta \leq 60°$ and θ increases in increments of 10°. Propellers with $n_b = 4$ and $\theta = 20°$ and $\theta = 30°$ were omitted as the required cord length was excessive. The blade height was set to be 30 mm and the cord length was chosen to be the dependent variable. Each propeller was designed to produce approximately 150 kW at maximum efficiency. Table 3 shows the cord length in mm for each combination of n_b and θ.

Table 3. The cord length in mm, which was required to produce 150 kW of thrust power with the given combinations of n_b and θ.

	n_b				
θ	**4**	**6**	**8**	**10**	**12**
20°	-	470	358	288	188
30°	-	235	178	144	100
40°	265	152	100	81	60
50°	165	90	63	47	36
60°	90	52	36	26.5	20

Two obvious trends can be observed in Table 3. The cord length required to produce 150 kW of thrust power increases non linearly with decreasing θ and n_b, respectively. It is, furthermore, reasonable to assume that, at each cord angle, the smaller the number of blades, the larger the power efficiency due to the increase in cord length.

In Figure 14, the peak efficiency of these propellers is plotted over the velocity ratio.

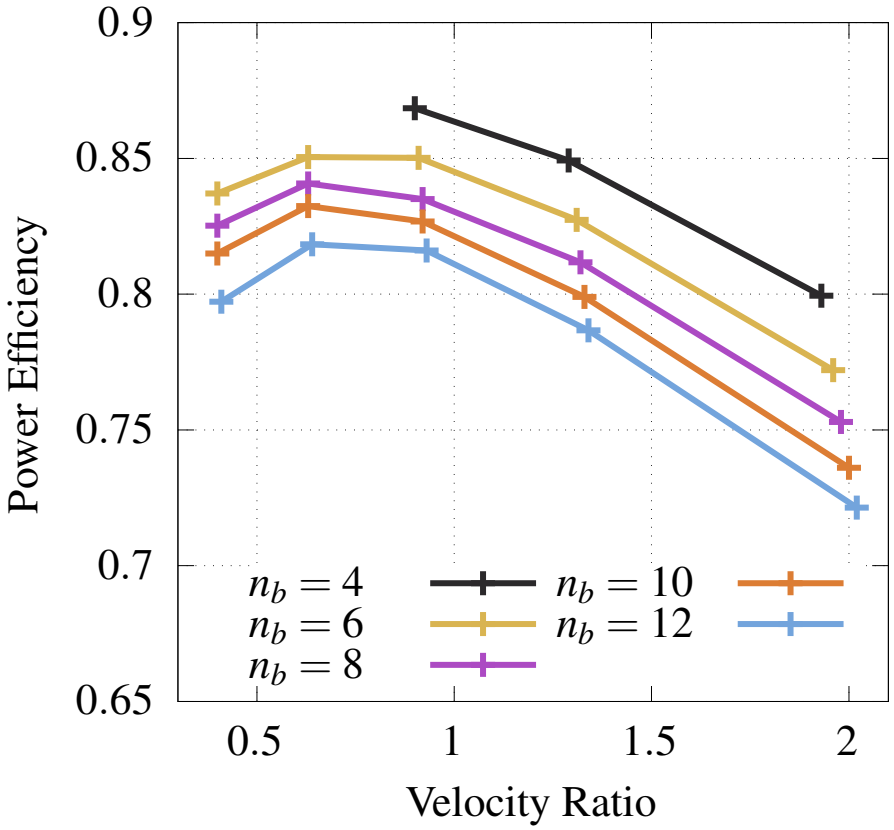

Figure 14. The power efficiency peaks of the 150 kW propellers.

Data points, which are approximately vertically aligned, are at the same cord angle. Note that, as expected, the smallest number of blades results in the largest power efficiency at each cord angle. Furthermore, note that the minimum power efficiency is well above 0.7. Hence, each propeller provides good performance. Comparing Figure 14 to Figure 9a, we can see that the efficiency maximum has shifted from between $\theta = 40°$ and $\theta = 50°$ to between $\theta = 30°$ and $\theta = 40°$ for each curve of constant n_b. This is because the increase in cord length compensates for the loss of efficiency from reducing θ. However, the opposite effect can be seen for $\theta > 40°$. Both the increase in θ and the decrease in cord length cause the efficiency to be reduced. The efficiency curves are thus steeper than in Figure 13.

Figure 15 shows the wall temperature on the windward side of the different blades. The leeward temperature is not shown since it is usually lower and transition occurs later. Clearly, neither $\theta = 50°$ nor $\theta = 60°$ satisfies the design constraints. At $\theta = 20°$, the blades have to be so long that the boundary layer transitions on each of them. In fact, only four blades satisfy both the temperature and the transition criterion, i.e., $\theta = 30°$ with $n_b = 12$ and $\theta = 40°$ with $n_b \geq 8$.

Since the hub radius has no bearing on blade performance with respect to the velocity ratio, the hub radius can be selected solely based on the required torque and maximum rotational frequency. In Figure 16, motor torque is plotted over its frequency for a variable hub radius for the remaining four blades.

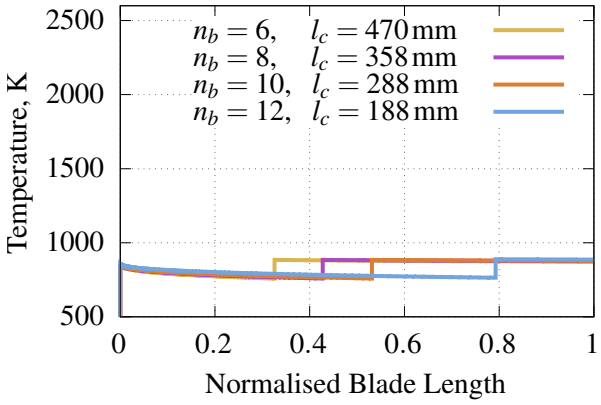

(**a**) $\theta = 20°$

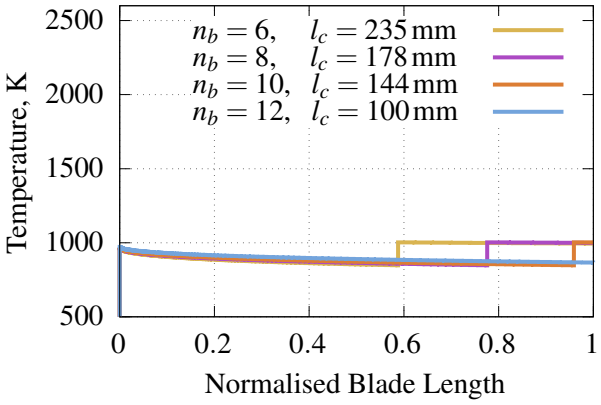

(**b**) $\theta = 30°$

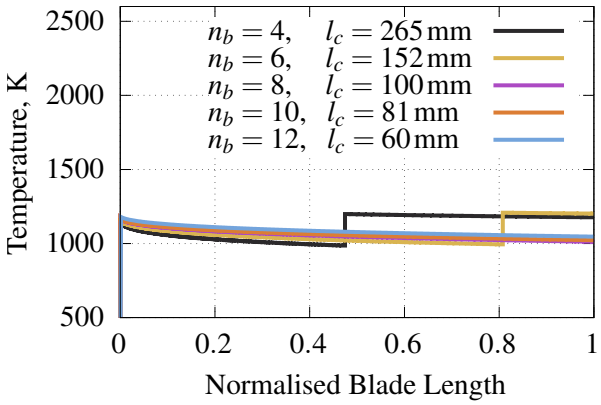

(**c**) $\theta = 40°$

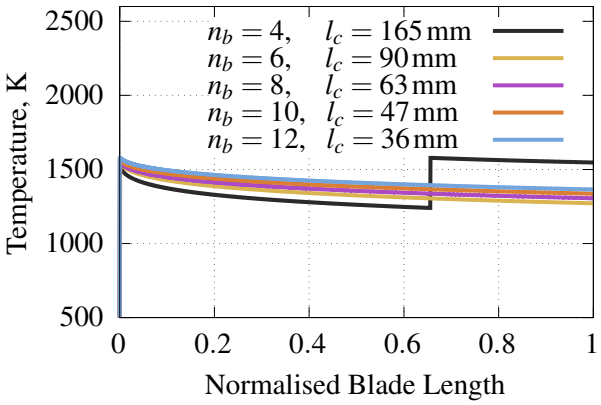

(**d**) $\theta = 50°$

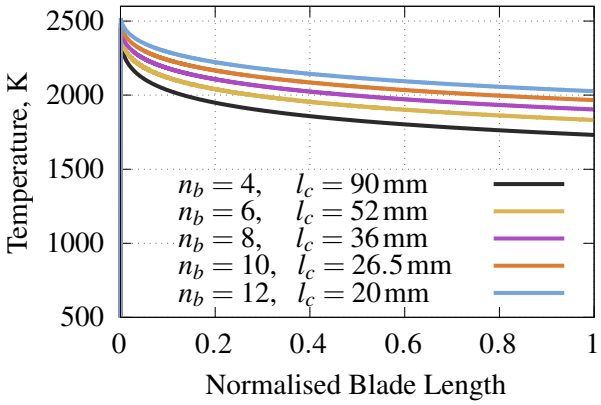

(**e**) $\theta = 60°$

Figure 15. Temperature profiles of the blades at (**a**) $\theta = 20°$, (**b**) $\theta = 30°$, (**c**) $\theta = 40°$, (**d**) $\theta = 50°$ and (**e**) $\theta = 60°$.

Both configurations with $n_b = 12$ sit just outside of the specified range. The best performing configuration, which meets all the design criteria, is, thus, the one with $n_b = 8$, $\theta = 40°$ and $l_c = 100$ mm. The required hub radius is 210 mm. The power efficiency of the propeller is thus 0.83.

At 95 % electric system efficiency the electric motor needs to produce approximately 190 kW and be able to store 8.9 kWh for a range of 200 km. With the values for specific power and specific energy cited in Section 1, a 27 kg battery is needed to meet the power requirements and a 32 kg battery to meet the range constraint. This means that, currently, over 49 % of the vehicle mass will be occupied by the battery leaving 33 kg for the electric

motor with controller and the structure of the vehicle. The overall system efficiency of the designed propeller is 0.79.

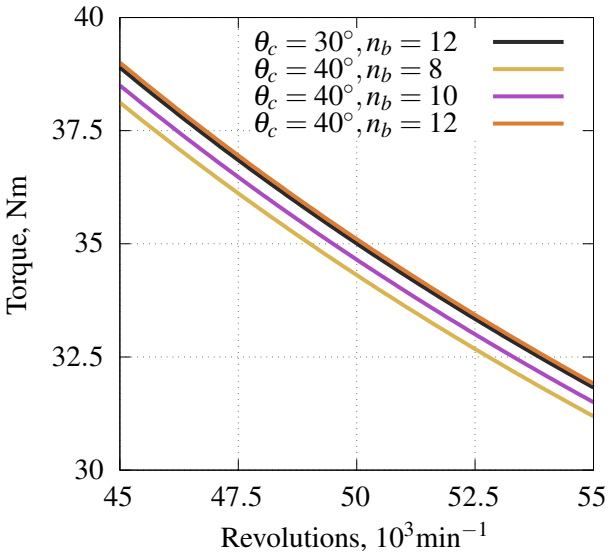

Figure 16. The torque of the electric motor over its frequency for the four remaining blades.

4. Discussion

A preliminary analysis of a supersonic electric propeller was performed. A two-dimensional flow model in conjunction with the reference temperature method was used to model the flow around the propeller and the blade temperature. The foremost conclusion of the analysis is that such a system is feasible from an aerodynamic and thermodynamic perspective, but further analysis is required. It was shown that a flat plate blade performs better than a diamond-shaped blade or a generic four-sided blade and that power efficiencies in excess of 0.8 are achievable. Furthermore, it was shown that power efficiencies above 0.6 can be achieved over a wide range of altitudes and Mach numbers, albeit with a variable cord angle. At about Mach 5.5 and 15 km altitude the temperature limit of contemporary materials is reached and further acceleration will result in the destruction of the propeller blades. Considering that an increase in velocity ratio is required to fly at higher altitudes, it stands to reason that Mach 5.5 cannot be exceeded at higher altitudes either.

It was demonstrated how the blade's geometric parameters affect its performance and that, in general, longer blades perform better. However, boundary layer transition affects longer blades and, with the current level of analysis, the consequences of transition cannot be assessed. The power efficiency maximum with respect to the cord angle of the blade was found to be between 40° and 50°. In the second part, a sample mission was specified and a propeller was designed to meet the requirements. It was shown that the assertions about the geometric parameters change once a propeller is designed for a specific purpose. The power efficiency maximum, for instance, sat in between 30° and 40°. However, the propeller with the fewest blades and, thus, with the biggest cord length, which satisfied all the design criteria, achieved the highest power efficiency.

Author Contributions: Conceptualization, A.P.; methodology, J.K. and A.P.; software, J.K.; validation, J.K. and A.P.; formal analysis, J.K.; investigation, J.K. and A.P.; resources, A.P.; data curation, J.K. and A.P.; writing—original draft preparation, J.K.; writing—review and editing, J.K. and A.P.; visualization, J.K.; supervision, A.P.; project administration, A.P.; funding acquisition, A.P. All authors have read and agreed to the published version of the manuscript.

Funding: This research was a collaboration between the Commonwealth of Australia (represented by the Defence Science and Technology Group) and the University of Queensland, through a Defence Science Partnerships agreement.

Data Availability Statement: The data presented in this study are openly available in UQ eSpace at https://doi.org/10.48610/9292b60.

Conflicts of Interest: The authors declare no conflict of interest.

References

1. Sherrill, S.A.; Banerjee, P.; Rubloff, G.W.; Lee, S.B. High to ultra-high power electrical energy storage. *Phys. Chem. Chem. Phys.* **2011**, *13*, 20714–20723. [CrossRef] [PubMed]
2. Ban, J.; Jiao, X.; Feng, Y.; Xue, J.; He, C.; Song, J. All-Temperature, High-Energy-Density Li/CF x Batteries Enabled by a Fluorinated Ether as a Cosolvent. *ACS Appl. Energy Mater.* **2021**, *4*, 3777–3784. [CrossRef]
3. Trocino, S.; Lo Faro, M.; Zignani, S.C.; Antonucci, V.; Aricò, A.S. High performance solid-state iron-air rechargeable ceramic battery operating at intermediate temperatures (500–650 °C). *Appl. Energy* **2019**, *233–234*, 386–394. [CrossRef]
4. Li, P.; Deng, J.; Li, J.; Wang, L.; Guo, J. Hollow graphene spheres coated separator as an efficient trap for soluble polysulfides in Li-S battery. *Ceram. Int.* **2019**, *45*, 13219–13224. [CrossRef]
5. Park, S.H.; King, P.J.; Tian, R.; Boland, C.S.; Coelho, J.; Zhang, C.; McBean, P.; McEvoy, N.; Kremer, M.P.; Daly, D.; et al. High areal capacity battery electrodes enabled by segregated nanotube networks. *Nat. Energy* **2019**, *4*, 560–567. [CrossRef]
6. Shelar, S. Groundwork for the Development of a Plasma Fuelled Engine. Master's Thesis, Centre for Hypersonics, School of Mechanical and Mining Engineering, The University of Queensland, Brisbane, Australia, 2021.
7. Raza, W.; Ali, F.; Raza, N.; Luo, Y.; Kim, K.H.; Yang, J.; Kumar, S.; Mehmood, A.; Kwon, E.E. Recent advancements in supercapacitor technology. *Nano Energy* **2018**, *52*, 441–473. [CrossRef]
8. Staff, A.R. *Equations, Tables and Charts for Compressible Flow*; Technical Report NACA RP 1135; National Advisory Committee for Aeronautics: Boston, MA, USA, 1953.
9. Meador, W.E.; Smart, M.K. Reference Enthalpy Method Developed from Solutions of the Boundary-Layer Equations. *AIAA J.* **2005**, *43*, 135–139. [CrossRef]
10. Hirschel, E.H.; Cousteix, J.; Kordulla, W. *Three-Dimensional Attached Viscous Flow*; Springer: Berlin, Heidelberg, 2014. [CrossRef]
11. McBride, B.J.; Gordon, S. *Computer Program for Calculation of Complex Chemical Equilibrium Compositions and Applications I. Analysis*; Technical Report NASA-RP-1311; NASA Lewis Reserach Center: Clevelend, OH, USA, 1994.
12. McBride, B.J.; Gordon, S. *Computer Program for Calculation of Complex Chemical Equilibrium Compositions and Applications II. Users Manual and Program Description*; Technical Report NASA-RP-1311; NASA Lewis Reserach Center: Clevelend, OH, USA, 1996.
13. Virtanen, P.; Gommers, R.; Oliphant, T.E.; Haberland, M.; Reddy, T.; Cournapeau, D.; Burovski, E.; Peterson, P.; Weckesser, W.; Bright, J.; et al. SciPy 1.0: Fundamental Algorithms for Scientific Computing in Python. *Nat. Methods* **2020**, *17*, 261–272. [CrossRef] [PubMed]
14. Coles, D. Measurements of Turbulent Friction on a Smooth Flat Plate in Supersonic Flow. *J. Aeronaut. Sci.* **1954**, *21*, 433–448. [CrossRef]
15. Chang, E.W.K. Hypersonic Shock Impingement Studies on a Flat Plate with Elevated Wall Temperatures. Ph.D. Thesis, Centre for Hypersonics, School of Mechanical and Mining Engineering, The University of Queensland, Brisbane, Australia, 2021. [CrossRef]
16. Kraft, D. Algorithm 733: TOMP–Fortran Modules for Optimal Control Calculations. *ACM Trans. Math. Softw.* **1994**, *20*, 262–281. [CrossRef]
17. Anderson, J.D.; Lewis, M.J.; Kothari, A.P.; Corda, S. Hypersonic Waveriders for Planetary Atmospheres. *J. Spacecr. Rocket.* **1991**, *28*, 401–410. [CrossRef]